This is a preprint, the final version is subject to change, of the American Mineralogist (MSA)
Cite as Authors (Year) Title. American Mineralogist, in press.
DOI: https://doi.org/10.2138/am-2020-7403

Revision 1

Experimental constraints on the partial melting of sediment-metasomatized lithospheric mantle in subduction zones

Yanfei Zhang[1,3,*], Xuran Liang[2,3], Chao Wang[3], Zhenmin Jin[3], Lüyun Zhu[4], Wei Gan[5]

[1] College of Oceanography, Hohai University, Nanjing 210098, China

[2] Guangzhou Institute of Geochemistry, Chinese Academy of Sciences, Guangzhou 510640, China

[3] State Key Laboratory of Geological Processes and Mineral Resources, China University of Geosciences, Wuhan 430074, China

[4] School of Earth Resources, China University of Geosciences, Wuhan 430074, China

[5] School of Earth Sciences and Resources, China University of Geosciences, Beijing 100083, China

[*] Corresponding author: Y. Zhang

Email: yanfzhang@126.com

No. 1, Xikang road, Nanjing 210098, Jiangsu, China

No. 388, Lumo road, Wuhan 430074, Hubei, China

Abstract

Sedimentary diapirs can be relaminated to the base of the lithosphere during slab subduction, where they can interact with the ambient lithospheric mantle to form variably metasomatized zones. Here, high-pressure experiments in sediment-harzburgite systems were conducted at 1.5–2.5 GPa and 800–1300 ^{o}C to investigate the interaction between relaminated sediment diapirs and lithospheric mantle. Two end-member processes of mixed experiments and layered (reaction) experiments were explored. In the first end-member, sediment and harzburgite powders were mixed to a homogeneous proportion (1:3) whereas in the second, the two powders were juxtaposed as separate layers. In the first series of experiments, the run products were mainly composed of olivine + orthopyroxene + clinopyroxene + phlogopite in subsolidus experiments, while the phase assemblages were then replaced by olivine + orthopyroxene + melt (or trace phlogopite) in supersolidus experiments. Basaltic and foiditic melts were observed in all supersolidus mixed experiments (~44–52 wt% SiO_2 at 1.5 GPa, ~35–43 wt% SiO_2 at 2.5 GPa). In the phlogopite-rich experiment (PC431, 1.5 GPa and 1100 ^{o}C), the formed melts had low alkali contents (~<2 wt%) and K_2O/Na_2O ratios (~0.4–1.1). In contrast, the quenched melt in phlogopite-free/poor experiments showed relatively higher alkali contents (~4–8 wt%) and K_2O/Na_2O ratios (~2–5). Therefore, the stability of phlogopite could control the bulk K_2O and K_2O/Na_2O ratios of magmas derived from sediment-metasomatized lithospheric mantle. In layered experiments, a reaction zone

dominated by clinopyroxene + amphibole (or orthopyroxene) was formed because of the reaction between harzburgite and bottom sediment-derived melts (~62.5–67 wt% SiO_2). The total alkali contents and K_2O/Na_2O ratios of the formed melts were about 6–8 wt% and 1.5–3, respectively. Experimentally formed melts from both mixed and reaction experiments were rich in large ion lithosphile elements and displayed similar patterns with natural potassium-rich arc lavas from oceanic subduction zones (i.e., Mexian, Sunda, Central American and Aleutian). The experimental results demonstrated that bulk sediment diapirs, in addition to sediment melt, may be another possible mechanism to transfer material from a subducting slab to an upper mantle wedge or lithospheric mantle. On the other hand, the breakdown of phlogopite may play an important role in the mantle source that produces potassium-rich arc lavas in subduction zones.

Keywords: bulk sediment, lithosphere, partial melting, potassium-rich arc lava

1. Introduction

Subducted sediment is thought to have played an important role in creating mantle heterogeneity and the origin of potassium (K)-rich magmas in subduction zones (e.g., Tatsumi et al. 1986; Blundy and Sparks 1992; Prouteau et al. 2001). High-pressure experimental studies have demonstrated that subducted sediment may experience partial melting or dehydration because of heating from the surrounding mantle (e.g., Hermann and Spandler 2008; Hermann and Rubatto 2009; Castro et al. 2010; Mann and Schmidt 2015; Schmidt and Poli 2014; Schmidt 2015), which could release trace elements to the upper mantle wedge and contribute to the origin of arc lavas (e.g., Peacock 1990; Ulmer and Trommsdorff 1995; Shimoda et al. 1998; Bindeman et al. 2005; Duggen et al. 2007; Turner et al. 2012; Spandler and Pirard 2013; Kendrick et al. 2014; Harvey et al. 2014; Scambelluri et al. 2015; Shu et al. 2017). The recycling of sediment melt or fluid back into a mantle wedge has been demonstrated by matching the isotopic and trace element properties of sediment input and volcanic magma output (e.g., Plank and Langmuir 1993; Peate et al. 1997; Porter and White 2009; Turner et al. 2012).

Recent numerical simulations and geochemical analyses have revealed that subducted sediments could detach from a downgoing slab at temperatures of 500–850 ^{o}C to form buoyancy diapirs (Behn et al. 2011). Then, a portion of the cold diapir would rise buoyantly from the surface of the subducting slab and relaminate into the mantle beneath arc lavas (Hacker et al. 2011; Marschall and Schumacher 2012;

78 Maunder et al. 2016), where they would form a variety of mélanges through physical
79 mixing before arc magma generation (Marschall and Schumacher 2012; Nielsen and
80 Marschall 2017). On the other hand, geochemical analyses of alkaline arc lavas (very
81 low Nd/Sr at low $^{143}Nd/^{144}Nd$ values, $^{87}Sr/^{86}Sr$ ratios close to the depleted mantle)
82 have suggested that the composition of these arc lavas plot on the mixing line between
83 bulk sediment and mantle peridotite, rather than sediment melt and mantle peridotite
84 in Sr-Nd isotope space (Cruz-Uribe et al. 2018). Recently, Shu et al. (2017)
85 investigated the variation of arc lava Tl, Sr, Nd and Pb isotopes from the Ryukyu Arc
86 and Okinawa Trough; their results demonstrated that a mixing model between bulk
87 sediment (without trace element fractionation) and lithospheric mantle should be the
88 principle source of these arc lavas. Therefore, it was suggested that melting of
89 bulk-mixed mélange between sediment and lithospheric mantle/peridotite should be
90 an important transfer mechanism for the recycling of sediment components from a
91 subducting slab to arc lavas (Marschall and Schumacher 2012). On one hand,
92 sediment diapirs may react with mantle peridotite (lherzolite) at sub-arc depths (~80–
93 120 km); on the other hand, some sediment diapirs may be relaminated into the bottom
94 of lithospheric mantle because of buoyancy and react with lithospheric mantle
95 (harzburgite). There are two key issues concerning the partial melting phase relations
96 of sediment-harzburgite mélange and partial melt chemical compositions. Many
97 high-pressure experiments have been conducted to constrain the partial melting phase
98 relations in sediment + mid-oceanic ridge basalt (MORB) (Castro et al. 2010),

eclogite-derived melt + lherzolite (Mallik and Dasgupta 2013, 2014; Gervasoni et al. 2017), hydrous rhyolite + lherzolite (Mallik et al. 2015), sediment melt + lherzolite (Mallik et al. 2016), carbonate melt + lherzolite (Gervasoni et al. 2017), glimmerite + harzburgite (Förster et al. 2017), phyllite + dunite (Wang et al. 2017; Wang and Foley 2018), adakite + lherzolite (Corgne et al. 2018) and sediment-dominated mélange + lherzolite (Codillo et al., 2018). Those experimental results were mainly used to constrain melt-rock reaction processes at subarc depths and the origin of arc lavas in oceanic subduction zones. However, the metasomatism of lithospheric mantle by bulk sediment diapirs or the partial melting phase relations of sediment + harzburgite/dunite mélange is not completely understood because few experiments have been done (Förster et al. 2019a, b).

In this study, we conducted a series of experiments to examine the partial melting phase relations of sediment-harzburgite mélanges (mixed system vs. layered (reaction) system] at 1.5–2.5 GPa and 800–1300 ^{o}C, which corresponds to depths of ~45–75 km below the surface. The explored models assumed that a portion of sediment diapirs have been relaminated to the bottom of the lithospheric mantle during slab subduction and formed a variety of mélanges. The main purpose of this study was to investigate the effect of bulk sediment diapirs on the partial melting phase relations of mantle, and its implications for the origin of potassium-rich arc lavas.

2. Experimental details

2.1 Starting materials

The natural sediment sample (MSCS-3) used in this study was collected from the East China Sea continental shelf and is composed mainly of quartz, illite, chlorite and trace amounts of calcite (Wang et al. 2009). The volatile components in the sediment sample were mainly of H_2O (~4.9 wt%) and a small amount of CO_2 (~2.1 wt%). Both the major and trace element compositions of MSCS-3 were similar to global subducting sediment (GLOSS) (Plank and Langmuir 1998), except that it contained relatively higher concentrations of Al_2O_3 and lower concentrations of SiO_2 and CaO. The MSCS-3 powder was finely ground (~< 15 μm) in alcohol with an agate mortar. The harzburgite sample (Hz13) was synthesized by mixing approximately 82 wt% olivine with 18 wt% enstatite. The olivine and enstatite crystals were first hand-picked from a natural peridotite sample (DMP-018), then separately crushed into fine powder (~5–15 μm) and ground together in alcohol with an agate mortar to produce a homogeneous mixture. The mixed powder of the starting material (HS1A) was ground by mixing 25 wt% MSCS-3 with 75 wt% harzburgite in alcohol with an agate mortar to form a homogeneous fine powder. For reaction experiments, MSCS-3 was juxtaposed at the bottom of Hz13; the proportions of the two powders were roughly 1:1. Details of the starting material chemical compositions in this study and previous experiments are listed in Table 1.

2.2 Experimental techniques

High-pressure and high-temperature experiments were conducted at the laboratory for the Study of the Earth's Deep Interior (SEDI-Lab) at China University of Geosciences (Wuhan, China). Experiments at 1.5 GPa were carried out using a 150 ton non-end-loaded piston cylinder apparatus; experiments at 2.5 GPa were conducted in a 1000 ton multi-anvil press using 18/12 ((octahedral edge length/truncated edge length) cell assembly. For experiments conducted in the piston cylinder apparatus, the assembly consisted of a sample capsule placed between two MgO rods in a graphite heater, enclosed by a Pyrex and salt sleeve; the sample capsule was separated by a short MgO tube from the graphite heater (Wang et al. 2010). In terms of the 18/12 assembly, a ZrO_2 sleeve was placed inside of the spinel octahedron for thermal insulation and a graphite furnace was placed inside the ZrO_2 sleeve for heating; the sample capsule was placed inside a short MgO tube and sandwiched between two MgO rods. Type C thermocouples were used to measure the temperature at the center of the furnace without correcting for the effect of pressure on electromotive force. Au_{80}-Pd_{20} tubes were used as sample capsules. The capsules were first laser-sealed at one end, then the sample powders were loaded into the capsules, which were welded shut to avoid volatile release during the experiments. Experiments were terminated by switching off power to the furnace, quenching to below 200 ^{o}C within 10 s and then automatic decompression to atmospheric pressure.

2.3 Analytical techniques

The recovered samples were first polished for microstructure analysis using a scanning electron microscope (FE-SEM). Quantitative major element analyses of minerals and melts in the recovered samples were made on a JXA-8100 electron probe micro-analyzer (EPMA) using an accelerating voltage of 15 kV, a beam current of 20 nA and a beam size of 1–2 μm for minerals, and a beam current of 10 nA and a beam size of 5–30 μm for quench melts. The count times for measured elements were 10 s on peaks and 5 s on the background on each side of the peaks. The standard materials were diopside (Si, Mg and Ca), jadeite (Na), K-feldspar (K), pyrope (Al), Ca_5P_3F (P), hematite (Fe), $MnSiO_3$ (Mn), rutile (Ti), NiO (Ni) and eskolaite (Cr). The measurement errors were generally about 5% for elements of no more than 1 wt%, <1% for element concentrations of 1 wt% to 5 wt%, and <0.5% for elements contents of >5 wt%. Phase proportions in mixed experiments were estimated based on anhydrous mass balance calculations; minor oxides, such as Cr_2O_3, NiO and P_2O_5, were excluded. A spreadsheet package provided by Herrmann and Berry (2002) was used to calculate the mineral and melt weight proportions from major element compositions of bulk rock and each phase in the recovered samples. The amount of Fe-loss to the sample capsule was also estimated based on mass balance calculations. The calculated weight proportions of phases, uncertainties and residual errors are shown in Table 2.

Trace element contents of melt pools were measured by laser ablation inductively coupled plasma-mass spectrometry (LA-ICP-MS). The laser ablation system is GeoLas 2005, which is combining with an Angilent 7500a ICP-MS instrument at the

State Key Laboratory of Geological Processes and Mineral Resources (China University of Geosciences). All samples were measured in a time-resolved analysis mode and ablated by 193 nm laser under conditions of 5 J/cm^2 (energy density), 6 Hz (repetition rate) and 32 μm (spot size). More detailed information about operating conditions of the LA-ICP-MS are described in Zhu et al. (2013). Each analysis includes a background acquisition section of approximately 20–30 s (gas blank) and a data acquisition section of 50 s (sample). In this study, the combination data strategy of external standard calibration and internal standard is adopted for data calibration, in order to obtain accurate and precise element contents (Longerich et al. 1996; Mukherjee et al. 2014). In details, the international reference material NIST610 and U.S. Geological Survey reference glasses BIR-1G, BCR-2G, and BHVO-2G were used for data calibration of LA-ICP-MS analysis. The time-drift of the signal is corrected by linear interpolation (with time) according to the variations in NIST 610. Moreover, BCR-2G, BHVO-2G and BIR-1G were adopted as the external standards for the quantitative calibration. In general, off-line selection and integration of background and analytical signals along with time-drift correction and quantitative calibration were conducted using ICPMSDataCal (Liu et al. 2008).

3. Results

Back-scattered electron images of representative run products are shown in Figure 1. The stability range of mixed experiment phases in *P*-*T* space is shown in

Figure 2. Details of the experimental conditions and run products are summarized in Table 2 and the mineral and quench melt chemical compositions in all experiments are listed in Tables S1–S3 (supplementary data). In the reaction experiments, the analyzed melt pools were greater than ~200–300 μm in diameter; the quench melt chemical compositions were homogeneous because no quench crystals were found in the recovered charges. Therefore, representative melt compositions of both major and trace elements can be analyzed in large melt pools far away from the solid minerals. In most of the mixed experiments (Figure 1), re-crystallization textures were observed in quench melt pools. For EPMA analyses, large beam sizes (5–30 μm) were adopted to mitigate compositional errors associated with the quench textures, and representative values for each composition were obtained by averaging analytical points (n=15–21) in deferent regions of the sample capsules. In these experiments, the largest melt pools were usually no more than ~200 μm in diameter, which limited the LA-ICP-MS analyses as the laser spot had to be at least 32 μm in diameter. Reliable trace element compositions were obtained for melt pools greater than ~50–100 μm in diameter. Melt pools that were slightly smaller than ~50 μm (~30–50 μm) were also selected for LA-ICP-MS analyses, but no reliable data were obtained because the trace element compositions were easily contaminated by the surrounding solid phases. Each time-resolved spectrum was carefully checked for possible contamination by trace element-rich minerals. The analytical results in different domains showed

similar trace elements patterns, indicating that re-crystallization of quench melts had a small effect on trace element migration during experiment quenching.

3.1 Chemical equilibrium and the loss of iron in mixed experiments

In this study, reversal experiments were not conducted. In subsolidus experiments, variable Mg# [100*Mg/(Mg+Fe)] of olivine and orthopyroxene may indicate residual olivine crystals from the starting harzburgite that have not yet achieved Fe-Mg exchange equilibrium with the rest of the minerals in the sample. This is because a relatively lower temperature is adopted in those experiments, and it is very difficult to achieve equilibrium without a liquid diffusive medium. In supersolidus experiments, an approach to chemical equilibrium can be demonstrated by: (1) limited heterogeneity in mineral composition from core to rim and in different zones of the recovered sample capsule; (2) systematic changes in phlogopite composition as a function of temperature (Figure 3c–f); (3) systematic changes in olivine and orthopyroxene composition as a function of temperature ($\geq$ 1100 ^{o}C) (Figure 3a, b); (4) variations in olivine-melt and orthopyroxene-melt Fe^{2+}-Mg K_D from 0.16 to 0.33, which is roughly consistent with previous partial melting experiments in a sediment melt + lherzolite system ($K_D^{Fe\text{-}Mg}{}_{(Ol/Opx\text{-}melt)}$ = 0.2–0.4) (e.g., Mallik et al. 2016); (5) the sum of residual squares ranges from 0.1 to 2.0, which is low when considering the uncertainties in melt composition from average

heterogeneous quench phases. These criteria may imply that the experiments have approached chemical equilibrium.

The relative amount of Fe-loss to the sample capsule was calculated based on mass balance and varied from 17(1) to 32(1) % (Table 2). The relative Fe-loss in this study is consistent with previous studies in sediment melt + lherzolite systems (~10%–40%) that used $Au_{80}Pd_{20}$ or $Au_{75}Pd_{25}$ capsules (e.g., Mallik et al. 2015, 2016). Iron loss resulted in FeO deficiency in both the quench melt and solid phases. By assuming that the partition coefficient of FeO between the melt and other solid phases is not affected by Fe-loss, the deficiency of FeO in the quench melt can be calculated using the following equation: $FeO_{Def} = FeO_{Blost} / [D_{FeO}*(1-F)+F]$

where FeO_{Def} represents the deficiency of FeO from the melt composition, which can be added to measured melt FeO to obtain the FeO concentration of the melt prior to Fe-loss; FeO_{Blost} is the lost FeO from the bulk composition; D_{FeO} represents the bulk partition coefficient of FeO between the solid phases and melt, which can be calculated through the weight percent of each mineral and the mineral/melt partition coefficient of FeO; F is the weight proportion of melt.

3.2 Mixed experiments

In mixed experiments, the starting material was first transformed into an assemblage consisting of olivine + orthopyroxene + clinopyroxene + phlogopite and trace accessory minerals (i.e., magnesite, hematite, rutile, apatite and zircon) within a

265 temperature range of 800–1000 °C at 1.5 GPa (Table 2, Figure 2). When the
266 temperature was increased to 1100 °C, phlogopite and traces of melt were observed in
267 the run products (Figure 1a, c), indicating that the stability field of phlogopite is
268 greater than ~1100 °C at pressures of 1.5–2.5 GPa (Figure 2). For experiments
269 conducted at 1200–1300 °C, a fraction of quench melt was observed within
270 interparticles or along the sample capsules, but clinopyroxene and phlogopite were
271 not present in the run products (Figure 1b, d; Figure 2). The observation of magnesite
272 in the run products is consistent with the presence of trace amounts of carbonate in the
273 starting material; therefore, the quench melts may also contain traces of CO_2 because
274 no magnesite (or other carbonate phase) was detected in all supersolidus experiments.
275 Microprobe analyses provided compositional data for the coexisting phases in
276 the recovered experiments. Figure 3 shows the compositional variations of olivine,
277 orthopyroxene and phlogopite versus temperature at 1.5 GPa and 2.5 GPa. The Mg#
278 for olivine and orthopyroxene were corrected for Fe-loss by adding Fe to the resulting
279 experimental phases. The average Mg# of olivine and orthopyroxene in subsolidus
280 experiments was in the range of 88–90 and 87–89, respectively, while the Mg# of
281 olivine and orthopyroxene increased slightly with temperature in supersolidus
282 experiments (Figure 3a, b). As an important alkali-bearing phase, the concentrations
283 of K_2O and TiO_2 in phlogopite ranged from ~6–9 wt% and 0.4–1.6 wt%, respectively,
284 with temperatures from 800 °C to 1200 °C; while the Na_2O and NiO contents were
285 reduced from ~2 wt% to 1 wt% and ~0.4 wt% to 0.2 wt%, respectively, with

286 temperatures from 800 °C to 1100 °C (Figure 3c–f). Both alkali contents and
287 K_2O/Na_2O ratios for quench melts were lower at 1100 °C compared with 1200–1300
288 °C (Figure 3g, h), because a significant portion of K was contained by phlogopite
289 (PC431, ~8 wt%) that coexisted with melts in the run products.
290
291 **3.3 Reaction experiments**
292 In the reaction experiments, the sediment powder was juxtaposed at the bottom
293 of the harzburgite layer (Figure 1e). Three experiments were carried out at 1.5–2.5
294 GPa and 950–1000 °C to simulate the reaction between sediment-derived melt and
295 lithospheric mantle. In the run products, the bottom sediment powder was composed
296 mainly of melt + garnet and a small fraction of plagioclase or clinopyroxene. The
297 upper harzburgite layer mainly consisted of olivine + orthopyroxene, and trace
298 amounts of spinel. For experiments conducted at 950 °C and 1.5 GPa, a reaction zone
299 composed mainly of clinopyroxene and amphibole was observed between the
300 sediment-derived melt and harzburgite (Figure 1f), which was replaced by
301 orthopyroxene at 1000 °C and pressures of 1.5–2.5 GPa.
302
303 **3.4 Melt composition**
304 Melt compositions obtained using EPMA are shown in Figures 4–5. The FeO
305 concentrations in experimental melts were also corrected for Fe-loss by adding FeO to
306 melts, based on the partitioning of Fe between melt and other phases. Figure 4 shows

the SiO_2-(K_2O+Na_2O) diagram of melt compositions from both mixed and reaction experiments. In mixed experiments, melts formed at 1.5 GPa were mainly located within basalt and tephrite-trachybasalt regions in phlogopite-rich and phlogopite-free/poor experiments, respectively. In phlogopite-free/poor experiments, the experimental melts had total alkali contents and K_2O/Na_2O ratios of ~4–8 wt% and ~2–5, respectively. In phlogopite-rich experiment (i.e., PC431), the quench melt displayed SiO_2 concentrations of ~44–52 wt% with total alkali contents and K_2O/Na_2O ratios of ~0.7–3.7 wt% and ~0.4–1.1, respectively, because a significant portion of the bulk K_2O was contained by phlogopite in the residue phases. With a pressure increase to 2.5 GPa, the experimental melts were located in the foidite-tephrite zone, which displayed similar alkali concentrations and K_2O/Na_2O ratios to experimental melts from phlogopite-free/poor experiments at 1.5 GPa, but had relatively lower SiO_2 concentrations (~35–43 wt%). In reaction experiments, the resultant melts were mainly located within the dacite-trachydacite region, which showed SiO_2 concentrations of ~62.5–67 wt% and total alkalis and K_2O/Na_2O ratios of ~6–8 wt% and ~1.5–3, respectively. The quench melt compositions in phlogopite-rich (1.5 GPa) and reaction experiments belong to the subalkaline series, while experimental melts formed at 2.5 GPa are in the alkaline series.

Harker diagrams (Figure 5) were used to show the variations in major element compositions in this study. The Al_2O_3 concentrations in the quench melts showed weak correlations with increased SiO_2 (Figure 5a). In melts derived from mixed

328 experiments, the Al_2O_3 contents varied from ~16 wt% to 20 wt% at 1.5 GPa and
329 1100–1300 ^oC, which then decreased to ~12–17 wt% when pressure was increased to
330 2.5 GPa. In melts formed in reaction experiments, the average Al_2O_3 concentrations
331 were about 14.6–15.8 wt% at 1.5 GPa and 950–1000 ^oC, which then decreased to
332 about 13.4–13.8 wt% at 2.5 GPa and 1000 ^oC. Both MgO and FeO concentrations
333 decreased with an increase of SiO_2 (Figure 5b, c). In mixed experiments, the MgO
334 and FeO contents varied from ~10–19 wt% and ~6.5–9 wt%, respectively, at 2.5 GPa,
335 then decreased to ~1–10 wt% and ~2–7 wt%, respectively, at 1.5 GPa. In reaction
336 experiments, the experimental melts had the lowest MgO (~0.5–0.8 wt%) and FeO
337 (~1.2–1.8 wt%) concentrations (Figure 5b, c). The CaO, Na_2O and K_2O
338 concentrations in experimental melts showed weak correlations with increased SiO_2
339 and narrower variations of CaO and K_2O in reaction experiments compared with
340 mixed experiments (Figure 5d–f). In reaction experiments, the resultant melts had
341 relatively lower concentrations of MgO and FeO, indicating that they did not achieve
342 chemical equilibrium with the upper harzburgite layer, because the bottom sediment is
343 depleted in MgO and FeO with respect to harzburgite. The hybrid melts in mixed
344 experiments were rich in MgO and FeO, which may represent well-equilibrated
345 products in the residual solid phases.
346

347 **4. Discussion**

348 **4.1 Phlogopite stability in sediment-metasomatized lithospheric mantle**

Experimental results in phlogopite + diopside system (Sudo and Tatsumi 1990; Luth 1997), phlogopite-doped peridotite system (Fumagalli et al. 2009; Tumiati et al. 2013; Condamine and Médard 2014; Condamine et al. 2016), sediment melt + dunite/lherzolite system (Pirard and Hermann 2015; Mallik et al. 2015, 2016), sediment + dunite system (Förster et al. 2019a, b) and glimmerite + harzburgite system (Förster et al. 2017) have shown that phlogopite is an important K-bearing phase in metasomatized lithospheric mantle or mantle wedge. The stability field of phlogopite ranges from ~950 ^{o}C to >1300 ^{o}C at pressures of 1–3 GPa. For example, phlogopite was observed as a stable phase at temperatures of 800–1050 ^{o}C and 3.5 GPa in a sediment melt (25 wt%) + dunite (75 wt%) system (Pirard and Hermann 2015); while in a sediment melt (25 wt%) + lherzolite (75 wt%) system, phlogopite stability was thought to be ≤1250–1300 ^{o}C at 2–3 GPa (Mallik et al. 2015). In this study, phlogopite was observed at temperatures of no more than 1100–1200 ^{o}C (1.5–2.5 GPa) in mixed experiments. The stability field of phlogopite obtained in this study is roughly consistent with experiments conducted by Förster et al. (2017) and Condamine and Médard (2014) in glimmerite + harzburgite and phlogopite-doped peridotite systems, respectively. Figure 6 shows the variations of phase proportions in mixed sediment + harzburgite system as a function of temperature at 1.5 GPa. The proportion of olivine increased with temperature, accompanied by reductions in the orthopyroxene and phlogopite fractions. The disappearance of phlogopite and clinopyroxene was accompanied by the formation of quench melts, indicating that the

formation of potassium-rich melts should have a close relationship with the breakdown of phlogopite.

In oceanic subduction zones, potassium can be introduced into mantle wedges and lithospheric mantle through slab-derived fluid/melt, continental-derived sediment and phlogopite-bearing peridotite and form a variety of metasomatized zones (e.g., Foley 1992, 1993; Prelević et al. 2008; Wang and Foley 2018). Then, partial melting of the metasomatized peridotite may contribute to the origin of potassium-rich magmas in these regions. Therefore, it has been suggested that the breakdown or melting of phlogopite with increased temperature is essential for the generation of potassium-rich magmas in subduction zones and post-collisional settings (Wyllie and Sekine 1982; Foley et al. 1996; Prelević et al. 2012; Fritschle et al. 2013; Condamine and Médard 2014; Mallik et al. 2015). However, phlogopite was also thought to be unnecessary in a mantle source to produce potassium-rich magmas based on mixed experiments in phyllite + dunite system (Wang et al. 2017; Wang and Foley 2018). They suggested that potassium was introduced by the addition of continental-derived sediment via phengite; the breakdown of phengite could then release a significant amount of potassium into the resulting partial melt. Therefore, this phlogopite-free mantle source may be an alternative explanation for the generation of potassium-rich magmas in post-collisional settings (Wang et al. 2017; Wang and Foley 2018). Phengite is an important potassium-bearing phase in subducted sediment, oceanic crust and upper continental crust at depths ~<300 km below surface (*e.g.*, Schmidt

391 and Poli 1998; Ono 1998; Hermann and Green 2001; Hermann 2002; Hermann and
392 Spandler 2008; Wu et al. 2009). However, phengite has never been observed in mixed
393 experiments, such as andesite + lherzolite, sediment + MORB, sediment melt +
394 dunite/lherzolite, metasediment + dunite and sediment-dominated mélange +
395 lherzolite systems (*e.g.*, Castro et al. 2010; Mallik and Dasgupta 2014, Pirard and
396 Hermann 2015; Mallik et al. 2015, 2016; Codillo et al., 2018), because they have
397 compositions that are too high in Mg to produce phengite. In fact, neither phengite nor
398 phlogopite has been observed in all experiments conducted by Wang and Foley (2018)
399 in phyllite + dunite systems. We suggest that the absence of phlogopite or phengite in
400 those experiments may indicate a relationship with lower H_2O in the starting material
401 (0.88 wt%), which is not conducive to the formation of these K-bearing minerals
402 because they are hydrous phases. In addition, the limited temperature range (1000–
403 1100 ^{o}C) in Wang and Foley (2018) may also be related to the absence of phlogopite
404 or phengite in the run products, because phlogopite has been mostly observed as a
405 stable phase in subsolidus conditions and the stable field of phengite is usually less
406 than ~900 ^{o}C at <5 GPa (Schmidt and Poli 1998). After combining our experimental
407 results with previous studies (*e.g.*, Wyllie and Sekine 1982; Foley et al. 1996; Prelević
408 et al. 2012; Fritschle et al. 2013; Condamine and Médard 2014; Mallik et al. 2016),
409 we suggest that phlogopite is an important potassium-bearing phase in
410 sediment/sediment melt-metasomatized mantle at shallow depths because there is
411 little experimental evidence for the presence of phengite, although its presence is

412 unable to be ruled out completely by our experiments. With an increase in
413 temperature (or upwelling), the breakdown or melting of phlogopite may result some
414 potassium-rich melts. These melts could transport sediment signatures and potassium
415 into arc lavas in subduction zones or potassic magmas in post-collisional settings.
416
417 **4.2 Comparison of experimentally formed melts**
418 Experimental melts formed in sediment melt + lherzolite (Mallik et al. 2016),
419 sediment melt + dunite (Pirard and Hermann 2015), mélange + lherzolite (Codillo et
420 al. 2018), phyllite/sediment + dunite (Wang and Foley 2018; Förster et al. 2019a, b)
421 and mélange (Cruz-Uribe et al., 2018) systems were selected for comparison (Figure
422 5). If the mixed and reaction experiments are assumed to be two end-member
423 processes of slab material reacting with lithospheric mantle, a mixing of the resultant
424 melts in our experiments may show similar Al_2O_3 and FeO variations with melts
425 formed in mélange + lherzolite (Codillo et al. 2018) and sediment melt + dunite
426 (Pirard and Hermann 2015) systems (Figure 5a, c). The mixing line of MgO and CaO
427 in experimental melts from this study was roughly consistent with mélange-derived
428 melts (Figure 5b, d; Cruz-Uribe et al. 2018). The CaO concentrations in experimental
429 melts derived from mélange + lherzolite (Codillo et al. 2018) and sediment melt +
430 lherzolite (Mallik et al. 2016) systems were slightly higher than other experiments.
431 Experimental melts derived from mélange (Cruz-Uribe et al. 2018) and sediment melt
432 + dunite (Pirard and Hermann 2015) had slightly higher Na_2O compared with melts

433 from other experiments (Figure 5e). In terms of a phyllite + dunite system (Wang and
434 Foley 2018), the experimental melts exhibited relatively higher SiO_2 because the
435 starting material they use is rich in SiO_2 (~59 wt%). The composition of mélange +
436 lherzolite-derived melts (Codillo et al. 2018) displayed higher MgO and CaO and
437 lower Na_2O and K_2O than melts formed in a mélange system (Cruz-Uribe et al. 2018).
438 In a sediment + dunite system (Förster et al. 2019a, b), the experimental melts
439 exhibited lower concentrations of MgO and FeO (Figure 5b, c), because only layered
440 (reaction) experiments were conducted and the resulting melts may not have
441 equilibrated with the upper dunite layer (rich in MgO and FeO).

442 The N-MORB normalized trace element patterns of experimental melts in this
443 study are shown in Figure 7. Partial melts produced in mixed and reaction
444 experiments exhibited similar patterns for rare earth elements (REEs), large ion
445 lithosphile elements (LILEs) and high field strength elements (HFSEs), except for
446 slightly positive Zr-Hf anomalies in melts derived from reaction experiments (Figure
447 7). Recently, Wang and Foley (2018) found that melts formed in mixed experiments
448 are rich in heavy rare earth elements (HREEs) with respect to melts formed in
449 reaction experiments. This may be caused by the presence of higher proportions of
450 residual garnet in reaction experiments, which can preserve a significant portion of
451 the bulk rock HREE; therefore, the corresponding melts are poor in HREEs. The
452 mélange-derived melts exhibited similar trace element patterns with experimental
453 melts from this study (Figure 8a; Castro et al. 2010). Experimental melts formed in a

454 mélange + lherzolite system (Cruz-Uribe et al. 2018) displayed positive Zr-Hf
455 anomalies with respect to mélange-derived melts (Castro et al. 2010); this result may
456 indicate a relationship with relatively higher temperatures (Cruz-Uribe et al. 2018),
457 because it favors the breakdown of zircon and release of Zr-Hf to experimental melts.
458 In a sediment melt + lherzolite system (Mallik et al. 2016), the resultant melts
459 exhibited positive Sr and negative Th anomalies compared with melts in this study
460 (Figure 8b). Experimental melts formed in a phyllite + dunite system also showed
461 similar trace element patterns with melts derived from sediment + harzburgite, except
462 for relatively lower concentrations of HREEs and weak Zr-Hf anomalies (Figure 8c;
463 Wang and Foley 2018). The partial melts derived from reaction experiments between
464 sediment and dunite exhibited positive U and Ta anomalies compared with the melts
465 formed in this study (Figure 8c; Förster et al. 2019a). The melt/fluid from Pirard and
466 Hermann (2015) exhibited higher trace element concentrations and positive U, Ta, Sm
467 and Eu anomalies (Figure 8d); this result may be related to the relatively lower
468 temperatures they used, so that the proportions of the resulting melt/fluid were low
469 and the trace element concentrations in the melt/fluid were high.
470

471 **4.3 Recycling of sediment diapirs in subduction zones**

472 Major element compositions of natural potassium-rich arc lavas from the
473 Aleutian, Sunda, Central American and Mexian subduction zones were selected for
474 comparison with experimental melts (Figure 5). The potassium-rich arc data

475 (K_2O/Na_2O ratios of ≥1) were compiled from the GEOROC database
476 (http://georoc.mpch-mainz.gwdg.de). The mixing lines of melt composition between
477 mixed and reaction experiments are consistent with natural potassium-rich arc lavas in
478 SiO_2, Al_2O_3, MgO, K_2O and a portion of CaO and Na_2O (Figure 5a, b, d–f). At SiO_2
479 concentrations lower than ~51 wt% (Figure 5a), the Al_2O_3 in potassium-rich arc lavas
480 was slightly lower than experimentally formed melt in a sediment + harzburgite
481 system, but consistent with melt derived from sediment melt + lherzolite (Mallik et al.
482 2016). In addition, experimentally formed melts exhibited lower FeO concentrations
483 than potassium-rich arc lavas (Figure 5c); this result may be caused by crystal
484 fractionation in natural arc lavas during ascent to near-surface, because early
485 differentiation could simultaneously increase the total FeO content of the residue
486 magmas and reduce Al_2O_3 (e.g., Stakes et al. 1984). Therefore, it suggests that early
487 crystal fractionation of arc magmas could make variations in FeO and Al_2O_3 approach
488 the compositions of experimental-derived melts. The variations of CaO and Na_2O in
489 potassium-rich arc lavas are slightly higher than experimental melts obtained in this
490 study (Figure 5d, e), but consistent with melts derived from mélange (sediment +
491 oceanic crust) + lherzolite (Codillo et al. 2018) and sediment melt (CaO-Na_2O-rich) +
492 lherzolite (Mallik et al. 2016) systems. This may indicate that a variety of CaO and
493 Na_2O-rich components, such as oceanic crust, may be involved in the origins of such
494 arc lavas. Therefore, we suggest that recycled bulk sediment alone is insufficient to
495 explain the major element compositions of potassium-rich arc lavas; a variety of

basaltic crust (or melt derived from basaltic crust) components may also be involved in the mantle source of these arc lavas.

To further constrain the involvement of bulk sediment diapirs in the genesis of potassium-rich arc lavas, the trace element compositions of mixed and reaction melts in this study were compared with natural potassium-rich arc lavas from subduction zones (Figure 9). The trace element pattern of potassium-rich lavas from the Mexian and Sunda subduction zones are consistent with the melts derived from sediment + harzburgite experiments in this study (Figure 9a, b). The slightly positive Zr-Hf anomalies in some of the arc lavas from the Mexian subduction zone can be interpreted as melts from reaction experiments in sediment + harzburgite or sediment-dominated mélange systems (Figure 8a). For potassium-rich arc lavas from the Central American and Aleutian subduction zones, variations of Rb and Ba (or Th) are inconsistent with experimental melts from both mixed and reaction experiments (Figure 9c, d). This discrepancy can be explained by the involvement of mélange or sediment melt in the mantle source of these magmas (Figure 8a–b). The similar trace element patterns of melts derived from sediment + harzburgite experiments and natural potassium-rich arc lavas provide evidence for the involvement of bulk sediment diapirs in the mantle source of these arc lavas.

5. Implications

516 The transfer mechanisms of continental-derived sediments from a subducting
517 slab to the overlying mantle wedge or lithospheric mantle include
518 metamorphism-induced melts or fluids (Plank and Langmuir 1993; Peate et al. 1997;
519 Porter and White 2009; Turner et al. 2012; Pirard and Hermann 2015), bulk sediment
520 diapirs (Behn et al., 2011; Nielsen and Marschall 2017), and sediment-dominated
521 mélanges (Codillo et al. 2018; Cruz-Uribe et al. 2018); however, the dominant
522 transfer mechanism for this material is still debated. Previous studies have suggested
523 that bulk sediment diapirs can be introduced into the bottom of lithospheric mantle
524 during slab subduction and form variable mélanges. Relaminated sediment
525 components may significantly affect the physical and chemical properties of
526 lithosphere (harzburgite), because they have different major and trace element
527 compositions. Partial melting of these mélanges may result in magmas with different
528 potassium concentrations, depending on the stability or breakdown of phlogopite. The
529 new data from this study have revealed similar trace element patterns for the partial
530 melts derived from sediment + harzburgite mélanges and natural potassium-rich arc
531 lavas from subduction zones, indicating that bulk sediment diapirs may be a possible
532 transfer mechanism for slab material from a subducting plate to the upper mantle
533 wedge/lithospheric mantle. Therefore, these experimental data may help to understand
534 the partial melting phase relations of sediment-modified lithospheric mantle and
535 provide constraints on the evolution of lithosphere and the generation of
536 potassium-rich arc lavas in oceanic subduction zones.

Acknowledgments

We thank Jihao Zhu and Wei Li for technical support during EPMA analyses. We acknowledge the use of EPMA in the Key Laboratory of Submarine Geosciences, State Oceanic Administration. We thank Junlong Yang, Zhenjiang Wang, Xiangfa Wang, Juan Wang, Xingdong Zhou and Zhonghang Wang for technical support during high-pressure experiments and SEM analyses. We are grateful to Fred Davis, Ananya Mallik and two anonymous reviewers for their constructive suggestions and comments. Editorial handling by Don R. Baker and Sylvie Demouchy is greatly appreciated. This research was supported by the National Programme on Global Change and Air-Sea Interaction (GASI-GEOGE-02), National Natural Science Foundation of China (41772040, 91858104).

References

Behn, M.D., Kelemen, P.B., Hirth, G., Hacker, B.R., and Massonne, H.J. (2011) Diapirs as the source of the sediment signature in arc lavas. Nature Geoscience, 4, 641–646.

Bindeman, I.N., Eiler, J.M., Yogodzinski, G.M., Tatsumi, Y., Stern, C.R., Grove, T.L., Portnyagin, M., Hoernle, K., and Danyushevsky, L.V. (2005) Oxygen isotope evidence for slab melting in modern and ancient subduction zones. Earth and Planetary Science Letters, 235, 480–496.

558 Blundy, J.D., and Sparks, R.S.J. (1992) Petrogenesis of mafic inclusions in granitoids
559 of the Adamello Massif, Italy. Journal of Petrology, 33, 1039–1104.
560 Castro, A., Gerya, T., Garcia-Casco, A., Fernandez, C., Diaz-Alvarado, J.,
561 Moreno-Ventas, I., and Low, I. (2010) Melting relations of MORB-sediment
562 mélanges in underplated mantle wedge plumes: Implications for the origin of
563 cordilleran-type batholiths. Journal of Petrology, 51, 1267–1295.
564 Codillo, E.A., Le Roux, V., and Marschall, H.R. (2018) Arc-like magmas generated
565 by mélange-peridotite interaction in the mantle wedge. Nature Communications,
566 9(1), 2864.
567 Condamine, P., and Médard, E. (2014) Experimental melting of phlogopite-bearing
568 mantle at 1 GPa: Implications for potassic magmatism. Earth and Planetary
569 Science Letters, 397, 80–92.
570 Condamine, P., Médard, E., and Devidal, J.L. (2016) Experimental melting of
571 phlogopite-peridotite in the garnet stability field. Contributions to Mineralogy
572 and Petrology, 171(11), 95.
573 Corgne, A., Schilling, M.E., Grégoire, M., and Langlade, J. (2018) Experimental
574 constraints on metasomatism of mantle wedge peridotites by hybridized adakitic
575 melts. Lithos, 308-309, 213–226.
576 Duggen, S., Portnyagin, M., Baker, J., Ulfbeck, D., Hoernle, K., Garbe-SchoÅNnberg,
577 D., and Grassineau, N. (2007) Drastic shift in lava geochemistry in the
578 volcanic-front to near-arc region of the Southern Kamchatkan subduction zone:

579 Evidence for the transition from slab surface dehydration to sediment melting.
580 Geochimica et Cosmochimica Acta, 71, 452–480.
581 Foley, S.F. (1992) Vein-plus-wall-rock melting mechanisms in the lithosphere and the
582 origin of potassic alkaline magmas. Lithos, 28, 435–453.
583 Foley, S.F. (1993) An experimental study of olivine lamproite-first results from the
584 diamond stability field. Geochimica et Cosmochimica Acta, 57, 483–489.
585 Foley, S.F., Jackson, S.E., Fryer, B.J., Greenouch, J.D., and Jenner, G.A. (1996)
586 Trace element partition coefficients for clinopyroxene and phlogopite in an
587 alkaline lamprophyre from Newfoundland by LAM-ICP-MS. Geochimica et
588 Cosmochimica Acta, 604, 629–638.
589 Förster, M.W., Prelević, D., Buhre, S., Mertz-Kraus, R., and Foley, S.F. (2019a) An
590 experimental study of the role of partial melts of sediments versus mantle melts
591 in the sources of potassic magmatism. Journal of Asian Earth Sciences, 177, 76–
592 88.
593 Förster, M.W., Foley, S.F., Alard, O., and Buhre, S. (2019b) Partitioning of nitrogen
594 during melting and recycling in subduction zones and the evolution of
595 atmospheric nitrogen. Chemical Geology, 525, 334–342.
596 Förster, M.W., Prelević, D., Schmück, H.R., Buhre, S., Veter, M., Mertz-Kraus, R.,
597 Foley, S.F., and Jacob, D.E. (2017) Melting and dynamic metasomatism of
598 mixed harzburgite + glimmerite mantle source: Implications for the genesis of
599 orogenic potassic magmas. Chemical Geology, 455, 182–191.

600 Fritschle, T., Prelevic, D., Foley, S.F., and Jacob, D.E. (2013) Petrological
601 characterization of the mantle source of Mediterranean lamproites: Indications
602 from major and trace elements of phlogopite. Chemical Geology, 353, 267–279.
603 Fumagalli, P., Zanchetta, S., and Poli, S. (2009) Alkali in phlogopite and amphibole
604 and their effects on phase relations in metasomatized peridotites: a high-pressure
605 study. Contributions to Mineralogy and Petrology, 158, 723–737.
606 Gervasoni, F., Klemme, S., Rohrbach, A., Grützner, T., and Berndt, J. (2017)
607 Experimental constraints on mantle metasomatism caused by silicate and
608 carbonate melts. Lithos, 282-283, 173–186.
609 Hacker, B.R., Kelemen, P.B., and Behn, M.D. (2011) Differentiation of the
610 continental crust by relamination. Earth and Planetary Science Letters, 307,
611 501–516.
612 Harvey, J., Garrido, C.J., Savov, I., Agostini, S., PadroÅLn-Navata, J.A., Marchesi,
613 C., SaÅLnchez-VizcaıÅLno, V.L., and GoÅLmez-Pugnaire, M.T. (2014)
614 ^{11}B-rich fluids in subduction zones: The role of antigorite dehydration in
615 subducting slabs and boron isotope heterogeneity in the mantle. Chemical
616 Geology, 376, 20–30.
617 Hermann, J. (2002) Experimental constraints on phase relations in subducted
618 continental crust. Contributions to Mineralogy and Petrology, 143, 219–235.

619 Herrmann, W., and Berry, R.F. (2002) MINSQ—a least squares spreadsheet method
620 for calculating mineral proportions from whole rock major element analyses.
621 Geochemistry: Exploration, Environment, Analysis, 2, 361–368.
622 Hermann, J., and Green, D.H. (2001) Experimental constraints on high pressure
623 melting in subducted crust. Earth and Planetary Science Letters, 188, 149–168.
624 Hermann, J., and Rubatto, D. (2009) Accessory phase control on the trace element
625 signature of sediment melts in subduction zones. Chemical Geology, 265, 512–
626 526.
627 Hermann, J., and Spandler, C.J. (2008) Sediment melts at sub-arc depths: An
628 experimental study. Journal of Petrology, 49, 717–740.
629 Kendrick, M.A., Arculus, R.J., and Danyushevsky, L.V. (2014) Subduction-related
630 halogens (Cl, Br, and I) and H_2O in magmatic glasses from Southwest Pacific
631 Backarc Basins. Earth and Planetary Science Letters, 400, 165–176.
632 Liu, Y., Hu, Z., Gao, S., Günther, D., Xu, J., Gao, C., and Chen, H. (2008) In situ
633 analysis of major and trace elements of anhydrous minerals by LA-ICP-MS
634 without applying an internal standard. Chemical Geology, 257, 34–43.
635 Longerich, H.P., Jackson, S.E., and Günther, D. (1996) Laser ablation inductively
636 coupled plasma mass spectrometric transient signal data acquisition and analyte
637 concentration calculation. Journal of Analytical Atomic Spectrometry, 11(9),
638 899–904.

639 Luth, R.W. (1997) Experimental study of the system phlogopite diopside from 3.5 to
640 17 GPa. American Mineralogist, 82, 1198–1209.
641 Mallik, A., and Dasgupta, R. (2013) Reactive infiltration of MORB-eclogite derived
642 carbonated silicate melt into fertile peridotite at 3 GPa and genesis of alkalic
643 magmas. Journal of Petrology, 54, 2267–2300.
644 Mallik, A., and Dasgupta, R. (2014) Effect of variable CO_2 on eclogite derived
645 andesite and lherzolite reaction at 3 GPa: Implications for mantle source
646 characteristics of alkalic ocean island basalts. Geochemistry Geophysics
647 Geosystems, 15, 1533–1557.
648 Mallik, A., Dasgupta, R., Tsuno, K., and Nelson, J. (2016) Effects of water, depth and
649 temperature on partial melting of mantle-wedge fluxed by hydrous
650 sediment-melt in subduction zones. Geochimica et Cosmochimica Acta, 195,
651 226–243.
652 Mallik, A., Nelson, J., and Dasgupta, R. (2015) Partial melting of fertile peridotite
653 fluxed by hydrous rhyolitic melt at 2–3 GPa: Implications for mantle wedge
654 hybridization by sediment melt and generation of ultrapotassic magmas in
655 convergent margins. Contributions to Mineralogy and Petrology, 169, 48.
656 Marschall, H.R., and Schumacher, J.C. (2012) Arc magmas sourced from mélange
657 diapirs in subduction zones. Nature Geoscience, 5, 862–867.
658 Maunder, B., and van Hunen, J. (2016) Relamination of mafic subducting crust
659 throughout Earth's history. Earth and Planetary Science Letters, 449, 206–216.

660 Mukherjee, P.K., Khanna, P.P., and Saini, N.K. (2014) Rapid determination of trace
661 and ultra trace level elements in diverse silicate rocks in pressed powder pellet
662 targets by LA-ICP-MS using a matrix-independent protocol. Geostandards and
663 Geoanalytical Research, 38 (3), 363–379.
664 Nielsen, S.G., and Marschall, H.R. (2017) Geochemical evidence for mélange melting
665 in global arcs. Science Advance, 3, e1602402.
666 Ono, S. (1998) Stability limits of hydrous minerals in sediment and mid-ocean ridge
667 basalt compositions: Implications for water transport in subduction zones.
668 Journal of Geophysical Research, 103, 18253–18267.
669 Peate, D.W., Pearce, J.A., Hawkesworth, C.J., Colley, H., Edwards, C.M.H., and
670 Hirose, K. (1997) Geochemical variations in Vanuatu arc lavas: The role of
671 subducted material and a variable mantle wedge composition. Journal of
672 Petrology, 38, 1331–1358.
673 Pirard, C., and Hermann, J. (2015) Experimentally determined stability of alkali
674 amphibole in metasomatised dunite at sub-arc pressures. Contributions to
675 Mineralogy and Petrology, 169, 1–26.
676 Plank, T., and Langmuir, C.H. (1993) Tracing trace elements from sediment input to
677 volcanic output at subduction zones. Nature, 362, 739–743.
678 Plank, T., and Langmuir, C.H. (1998) The chemical composition of subducting
679 sediment: implications for the crust and mantle. Chemical Geology, 145, 325–
680 394.

Porter, K.A., and White, W.M. (2009) Deep mantle subduction flux. Geochemistry Geophysics Geosystems, 10, 1–23.

Prelević, D., Foley, S.F., Romer, R., and Conticelli, S. (2008) Mediterranean tertiary lamproites derived from multiple source components in post-collisional geodynamics. Geochimica et Cosmochimica Acta, 72, 2125–2156.

Prelević, D., Akal, C., Foley, S.F., Romer, R.L., Stracke, A., and van den Bogaard, P. (2012) Ultrapotassic mafic rocks as geochemical proxies for post-collisional dynamics of orogenic lithospheric mantle: The case of southwestern Anatolia, Turkey. Journal of Petrology, 53, 1019–1055.

Prouteau, G., Scaillet, B., Pichavant, M., and Maury, R. (2001) Evidence for mantle metasomatism by hydrous silicic melts derived from subducted oceanic crust. Nature, 410, 197–200.

Scambelluri, M., Pettke, T., and Cannaò, E. (2015) Fluid-related inclusions in Alpine high-pressure peridotite reveal trace element recycling during subduction-zone dehydration of serpentinized mantle (Cima di Gagnone, Swiss Alps). Earth and Planetary Science Letters, 429, 45–59.

Schmidt, M.W. (2015) Melting of pelitic sediments at subarc depths: 2. Melt chemistry, viscosities and a parameterization of melt composition. Chemical geology, 404, 168–182.

Schmidt, M.W., and Poli, P. (1998) Experimentally based water budgets for dehydrating slabs and consequences for arc magma generation. Earth and Planetary Science Letters, 163, 361–379.

Schmidt, M.W., and Poli, S. (2014) Devolatilization during subduction. In H.H.D. Holland, K.K. Turekian, Ed., Treatise on Geochemistry (Second Edition), p. 669–701, Pergamon, Oxford.

Shimoda, G., Tatsumi, Y., Nohda, S., Ishizaka, K., and Jahn, B.M. (1998) Setouchi high-Mg andesites revisited: Geochemical evidence for melting of subducting sediments. Earth and Planetary Science Letters, 160, 479–492.

Shu, Y., Nielsen, S.G., Zeng, Z., Shinjo, R., Blusztajn, J., Wang, X., and Chen, S. (2017) Tracing subducted sediment inputs to the Ryukyu arc-Okinawa Trough system: Evidence from thallium isotopes. Geochimica et Cosmochimica Acta, 217, 462–491.

Spandler, C., and Pirard, C. (2013) Element recycling from subducting slabs to arc crust: A review. Lithos, 170-171, 208–223.

Stakes, D.S., Shervais, J.W. and Hopson, C.A. (1984) The volcanic-tectonic cycle of the FAMOUS and AMAR Valleys, Mid-Atlantic Ridge (36°47′N): Evidence from basalt glass and phenocryst compositional variations for a steady state magma chamber beneath the valley midsections, AMAR 3. Journal of Geophysical Research: Solid Earth, 89, 6995–7028.

720 Sudo, A., and Tatsumi, Y. (1990) Phlogopite and K-amphibole in the upper mantle:
721 Implication for magma genesis in subduction zones. Geophysics Research Letter,
722 17, 29–32.
723 Tatsumi, Y., Hamilton, D.L., and Nesbitt, R.W. (1986) Chemical characteristics of
724 fluid phase released from a subducted lithosphere and origin of arc magmas:
725 Evidence from high-pressure experiments and natural rocks. Journal of
726 Volcanology and Geothermal Research, 29, 293–309.
727 Tumiati, S., Fumagalli, P., Tiraboschi, C., and Poli, S. (2013) An experimental study
728 on COH-bearing peridotite up to 3·2GPa and implications for crust–mantle
729 recycling. Journal of Petrology, 54, 453–479.
730 Turner, S., Caulfield, J., Turner, M., van Keken, P., Maury, R., Sandiford, M., and
731 Prouteau, G. (2012) Recent contribution of sediments and fluids to the mantle's
732 volatile budget: Nature Geoscience, 5, 50–54.
733 Ulmer, P., and Trommsdorff, V. (1995) Serpentine stability to mantle depths and
734 subduction-related magmatism. Science, 268, 858–861.
735 Wang, C., Jin, Z., Gao, S., Zhang, J. and Zheng, S. (2010) Eclogite-melt/peridotite
736 reaction: Experimental constrains on the destruction mechanism of the North
737 China Craton. Science China: Earth Sciences, 53, 797–809.
738 Wang, X., Wang, Y., Gao, Y., Huang, Y., Wang, Z., and Shi, X. (2009) Preparation of
739 five China Sea and continental shelf sediment reference materials (MSCS-1–5)

with ultra-fineparticle size distributions. Geostandards and Geoanalytical Research, 33, 357–368.

Wang, Y., Foley, S.F., and Prelević, D. (2017) Potassium-rich magmatism from a phlogopite-free source. Geology, 45, 467–470.

Wang, Y., and Foley, S.F. (2018) Hybridization melting between continent-derived sediment and depleted peridotite in subduction zones. Journal of Geophysical Research: Solid Earth, 123, 3414–3429.

Wu, Y., Fei, Y., Jin, Z., and Liu, X. (2009) The fate of subducted Upper Continental Crust: An experimental study. Earth and Planetary Science Letters, 282, 275–284.

Wyllie, P.J., and Sekine, T. (1982) The formation of mantle phlogopite in subduction zone hybridization. Contributions to Mineralogy and Petrology, 79, 375–380.

Zhu, L., Liu, Y., Hu, Z., Hu, Q., Tong, X., Zong, K., Chen, H., and Gao S. (2013) Simultaneous Determination of Major and Trace Elements in Fused Volcanic Rock Powders Using a Hermetic Vessel Heater and LA-ICP-MS. Geostandards and Geoanalytical Research, 37(2), 207–229.

Figure captions

Figure 1. Backscattered electron images of representative run products. (a) and (b) Mixed experiments conducted at 1.5 GPa and 1100 ^{o}C (PC431) and 1.5 GPa and 1300 ^{o}C (PC463), respectively; melt + phlogopite or melt coexisting with olivine + orthopyroxene was observed in the run products. (c) Mixed experiment conducted at 2.5 GPa and 1100 ^{o}C (R908), showing that phlogopite and trace garnet coexisting with olivine and orthopyroxene. (d) Mixed experiment at 2.5 GPa and 1200 ^{o}C (R957), showing that an amount of quench melt was segregated along the sample capsule. (e) and (f) Reaction experiment carried out at 1.5 GPa and 950 ^{o}C (PC370), showing a reaction zone composed mainly of clinopyroxene and amphibole.

Figure 2. Experimental *P-T* phase diagram in the sediment + harzburgite system (mixed experiments). Major phases are shown in squares. The approximate solidus and stability limits of phlogopite were estimated from the experimental results.

Figure 3. Chemical compositions of minerals and melt in mixed experiments. (a) and (b) Variations of Mg# in olivine and orthopyroxene versus temperature; Fe-loss was corrected by adding Fe to olivine and orthopyroxene based on the partitioning of Fe between solid phases and melt. (c) to (f) Variations of Na_2O, K_2O, TiO_2 and NiO versus temperature in phlogopite. (g) and (h) Variations of K_2O+Na_2O and K_2O/Na_2O versus temperature in melts.

779

780 **Figure 4**. SiO_2-(K_2O+Na_2O) diagram of melt compositions obtained in both mixed
781 and reaction experiments. *R-exp*, melt in reaction experiments; *M-1.5(Phl)*, melt in
782 mixed experiments at 1.5 GPa with phlogopite in the residue minerals (PC431); *M-1.5*,
783 melt in mixed experiments at 1.5 GPa, phlogopite was not present or only very trace
784 amounts were present in the residue phases (PC460, PC463); *M-2.5*, melt in mixed
785 experiments at 2.5 GPa, phlogopite was not present in the residue phases (R957,
786 R1010).

787

788 **Figure 5**. Major element compositions of experimental melts and potassium-rich arc
789 lavas from this study and literatures. Major element variations of (a) Al_2O_3, (b) MgO,
790 (c) FeO, (d) CaO, (e) Na_2O and (f) K_2O versus SiO_2 for experimental melts and
791 natural potassium-rich arc lavas. Mélange + lherzolite data were from Codillo et al.
792 (2018); mélange (Cruz-Uribe et al. 2018); sediment melt + lherzolite (Mallik et al.
793 2016); sediment melt + dunite (Pirard and Hermann 2015); phyllite + dunite (Wang
794 and Foley 2018); sediment + dunite (Förster et al. 2019a, b). Experimental melts
795 obtained in this study were corrected for Fe-loss, by adding FeO back to experimental
796 melts. The purple shadowed zone represents natural potassium-rich arc lavas with
797 K_2O/Na_2O ratios ≥1 from the Mexian, Sunda, Central American and Aleutian
798 subduction zones, compiled from the GEOROC database
799 (http://georoc.mpch-mainz.gwdg.de).

800

801 **Figure 6**. Weight proportions of the phases in mixed experiments versus temperature
802 at 1.5 GPa.

803

804 **Figure 7**. Normal mid-oceanic ridge basalt (N-MORB) normalized trace element
805 compositions of experimental melts. Data for N-MORB were from Sun and
806 McDonough (1989).

807

808 **Figure 8**. N-MORB normalized trace element compositions of experimental melts
809 from this study and literatures. Experimental melts in (a) mélange (Cruz-Uribe et al.
810 2018) or mélange + lherzolite (Codillo et al. 2018), (b) and (d) sediment melt +
811 lherzolite/dunite (Mallik et al. 2016; Pirard and Hermann 2015), (c) phyllite + dunite
812 (Wang and Foley 2018) and sediment + dunite (Förster et al. 2019a). Melts in
813 M-experiments/ R-experiments indicate melts from mixed/reaction experiments in
814 this study.

815

816 **Figure 9**. Comparison of trace element patterns in the experimental melts of this
817 study and natural potassium-rich arc lavas. Arc lavas from the (a) Mexian, (b) Sunda,
818 (c) Central American and (d) Aleutian subduction zones.

819

820
821

822 Table 1. Compositions of starting materials used in this study and previous reports.

	MSCS-3	GLOSS	Hz13	HS-1A	SPMHKLB4	SPMHKLB6	Wang18	PER-SED	PH-high	PH-low
SiO_2	57.72	58.57	43.86	47.20	51.81	50.44	59.43	47.80	48.60	47.03
TiO_2	0.80	0.62	0.04	0.23	0.22	0.21	0.37	0.28	0.13	0.11
Al_2O_3	16.95	11.91	0.72	4.78	6.37	5.81	5.90	5.83	3.47	2.72
Cr_2O_3	-	-	0.06	0.05	0.24	0.26	0.19	-	-	-
FeO^T	6.08	5.21	9.23	8.44	6.38	6.73	5.88	7.27	6.93	6.92
MnO	0.21	0.32	0.14	0.16	0.10	0.12	0.10	0.13	0.09	0.10
MgO	2.74	2.48	45.46	34.78	29.70	31.56	25.32	33.40	37.42	37.42
CaO	2.82	5.95	0.08	0.77	2.54	2.64	0.90	4.06	0.23	0.33
Na_2O	2.57	2.43	0.01	0.65	1.02	0.89	0.84	0.89	0.53	1.21
K_2O	3.40	2.04	-	0.85	1.61	1.31	0.95	0.33	1.51	0.73
P_2O_5	0.18	0.19	-	0.05	0.05	0.04	-	0.01	-	-
LOI	7.02	10.30	-	1.76	4.00	6.00	0.88	0.34	1.25	3.75
Total	100.00	100.02	99.60	99.70	104.04	106.01	100.73	100.35	100.15	100.31

823 *HS-1A*, the hybrid sample powder used in this study, synthesized by mixing 25 wt% sediment (MSCS-3) with 75
824 wt% harzburgite (Hz13).
825 *SPMHKLB4* and *SPMHKLB6*, synthesized by mixing 25 wt% sediment-melt with 75 wt% lherzolite, from Mallik
826 et al. (2016).
827 *Wang18*, synthesized by mixing 50 wt% phyllite with 50 wt% dunite, from Wang et al. (2018).
828 *PER-SED*, synthesized by mixing 15 wt% mélange with 85 wt% lherzolite, from Codillo et al. (2018).
829 *PH-high* and *PH-low*, synthesized by mixing 25 wt% sediment-melt with 75 wt% olivine, from Pirard and
830 Hermann (2015).
831 FeO^T, total Fe was calculated as FeO.
832

833 Table 2. Summary of experimental conditions and run products.

Run	T	P	D	Geometry	Phase Modes (wt%)								
no.	(°C)	(GPa)	(hrs)		Ol	Opx	Cpx	Phl	Grt	melt	$\sum r^2$	Fe-loss	other minerals
PC307	800	1.5	113	Mixture	29(2)	54(2)	4(2)	12(1)			0.7±0.5	19(2)	Mag, Hem, Rut
PC322	900	1.5	72	Mixture	30(3)	53(3)	5(2)	11(1)			0.6±0.2	23(3)	Mag, Hem, Apa
PC368	950	1.5	60	Mixture	31(2)	49(2)	7(1)	12(1)			0.3±0.3	18(0)	Mag, Hem, Zir
PC365	1000	1.5	48	Mixture	32(3)	52(4)	6(2)	11(2)			0.3±0.1	17(1)	Mag, Hem,
PC431	1100	1.5	48	Mixture	34(3)	51(4)		8(1)		5(1)	0.3±0.1	17(1)	Mag
PC460	1200	1.5	53	Mixture	35(1)	50(1)				13(1)	0.2±0.1	26(1)	
PC463	1300	1.5	44	Mixture	46(2)	35(5)				18(3)	1.0±1.0	23(5)	
R908	1100	2.5	30	Mixture	27(1)	56(1)		9(1)	7(1)	‡	0.4±0.1	21(1)	
R957	1200	2.5	26	Mixture	34(1)	52(2)		‡		14(3)	0.3±0.1	18(2)	
R1010	1300	2.5	30	Mixture	32(3)	46(3)				21(2)	0.2±0.1	32(1)	
PC370	950	1.5	53	Layer	Harzburgite: Ol + Opx + Sp; Sediment: Grt + Pl + melt; Reaction zone: Cpx + Amp;								
PC478	1000	1.5	48	Layer	Harzburgite: Ol + Opx; Sediment: Grt + Cpx + melt; Reaction zone: Opx								
R1028	1000	2.5	30	Layer	Harzburgite: Ol + Opx; Sediment: Grt + melt; Reaction zone: Opx								

834 Mass balance calculations were performed to estimate the phase proportions (wt%) in mixed experiments.

835 ‡, Indicates trace presence of a phase which could not be detected by mass balance.

836 $\sum r^2$, Sum of residual square.

837 Fe-loss, Indicates the relative Fe-loss to the Au-Pd capsules with respective to the bulk Fe concentration in the

838 starting material, as estimated by mass balance.

839 Mineral abbreviations: *Ol*, olivine; *Opx*, orthopyroxene; *Cpx*, clinopyroxene; *Phl*, phlogopite; *Mag*, magnesite;

840 *Hem*, hematite; *Rut*, rutile; *Apa*, apatite; *Zir*, zircon; *Grt*, garnet; *Sp*, spinel; *Pl*, plagioclase; *Amp*, amphibole.

841

842

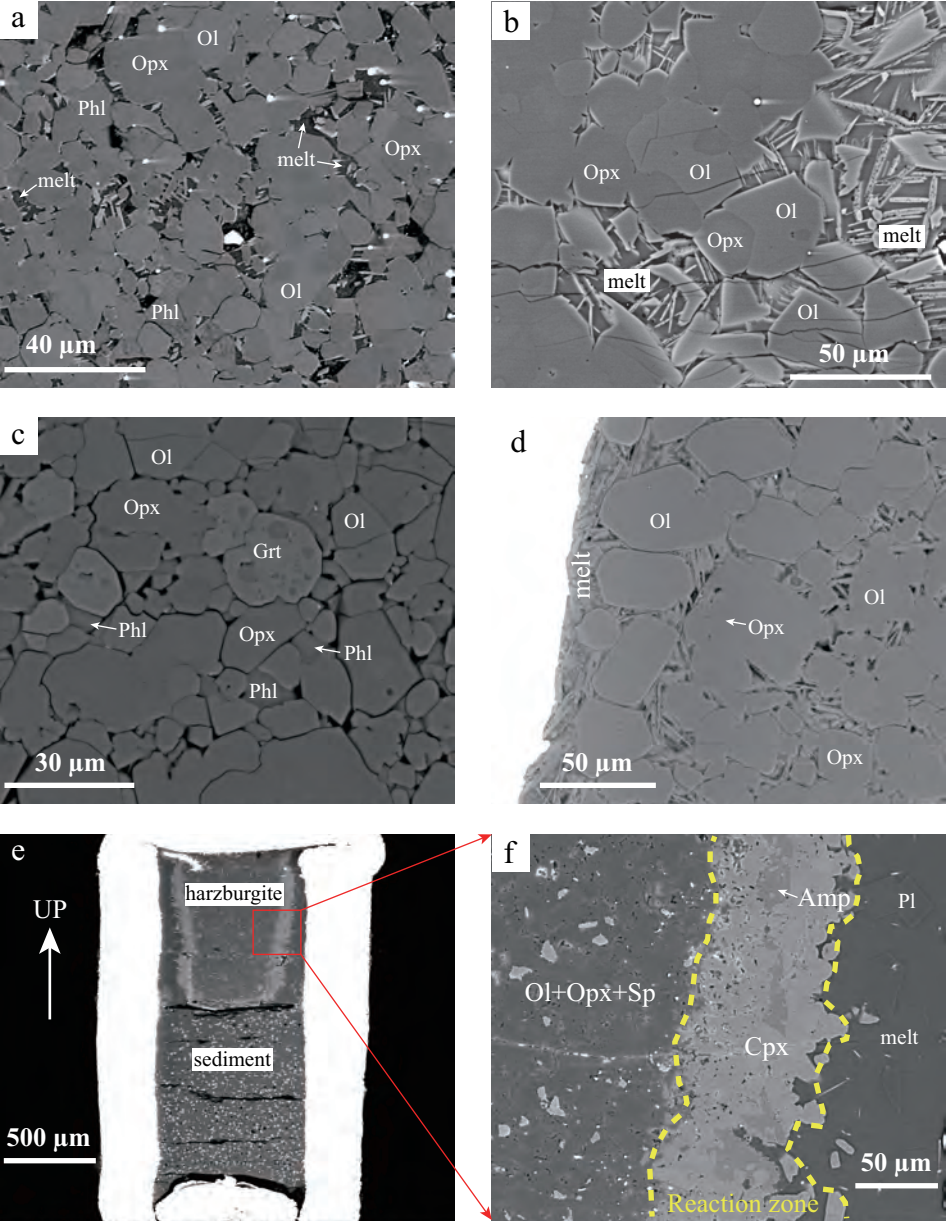
a
Ol
Opx
Phl
melt
Opx
melt
Ol
Phl
40 µm
b
Opx
Ol
Ol
Opx
melt
melt
Ol
50 µm
c
Ol
Opx
Ol
Grt
Phl
Opx
Phl
Phl
30 µm
d
Ol
melt
Ol
Opx
50 µm
Opx
e
UP
harzburgite
sediment
500 µm
f
Amp
Pl
Ol+Opx+Sp
Cpx
melt
50 µm
Reaction zone

Figure 1

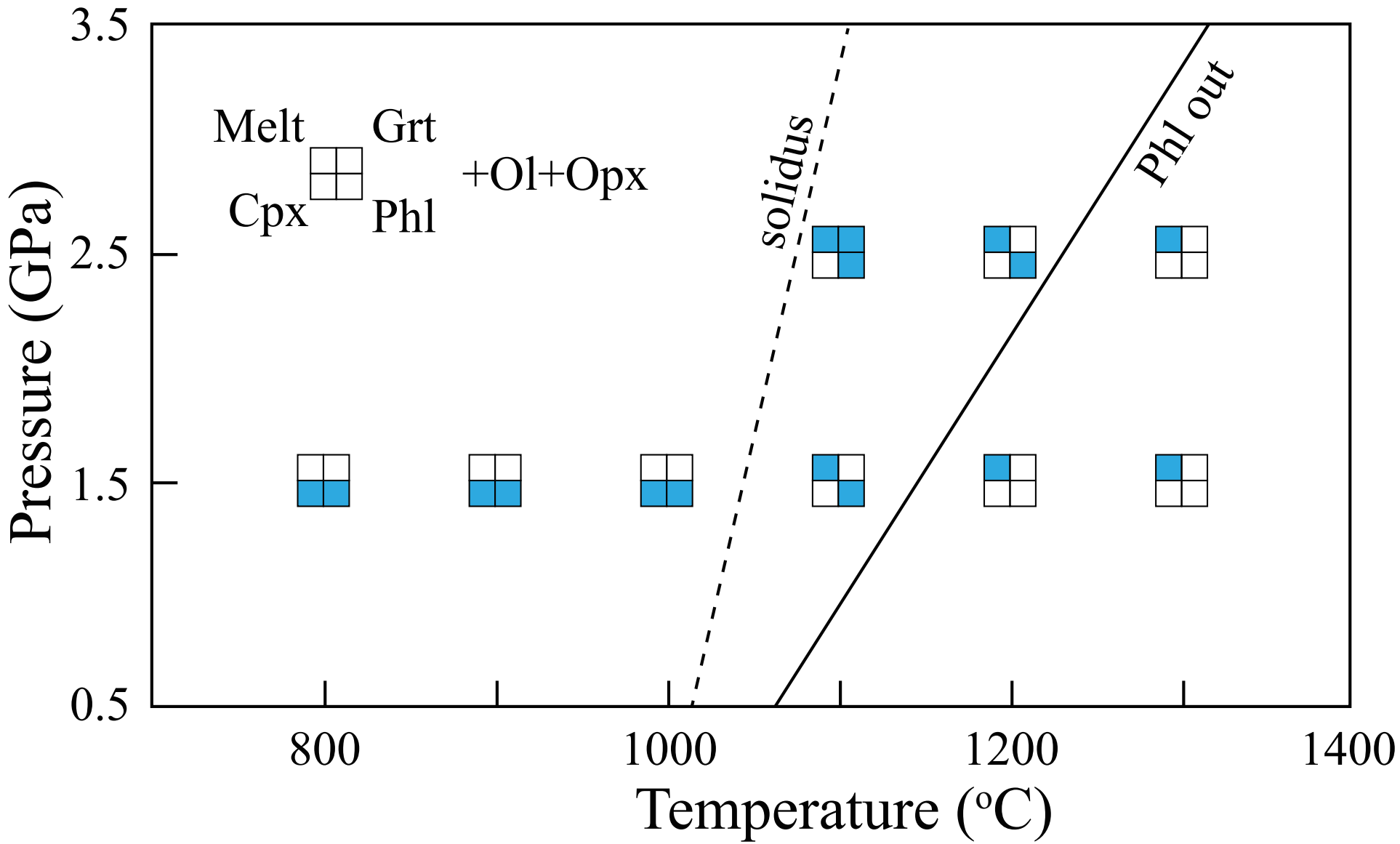
Melt
Grt
Cpx
Phl
+Ol+Opx
solidus
Phl out
Pressure (GPa)
3.5
2.5
1.5
0.5
800
1000
1200
1400
Temperature (°C)

Figure 2

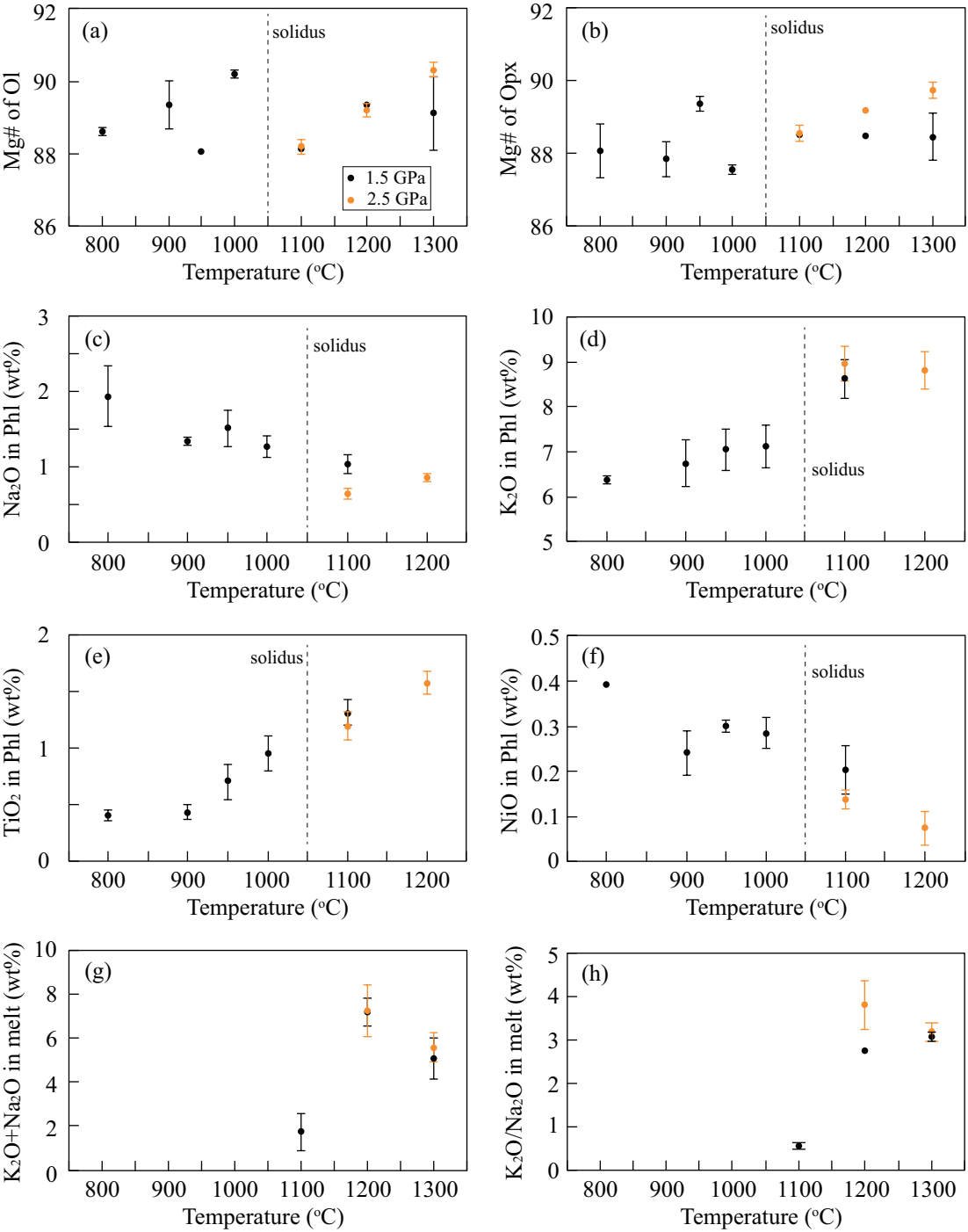
(a)
solidus
Mg# of Ol
1.5 GPa
2.5 GPa
Temperature (°C)
(b)
solidus
Mg# of Opx
Temperature (°C)
(c)
solidus
Na2O in Phl (wt%)
Temperature (°C)
(d)
solidus
K2O in Phl (wt%)
Temperature (°C)
(e)
solidus
TiO2 in Phl (wt%)
Temperature (°C)
(f)
solidus
NiO in Phl (wt%)
Temperature (°C)
(g)
K2O+Na2O in melt (wt%)
Temperature (°C)
(h)
K2O/Na2O in melt (wt%)
Temperature (°C)

Figure 3

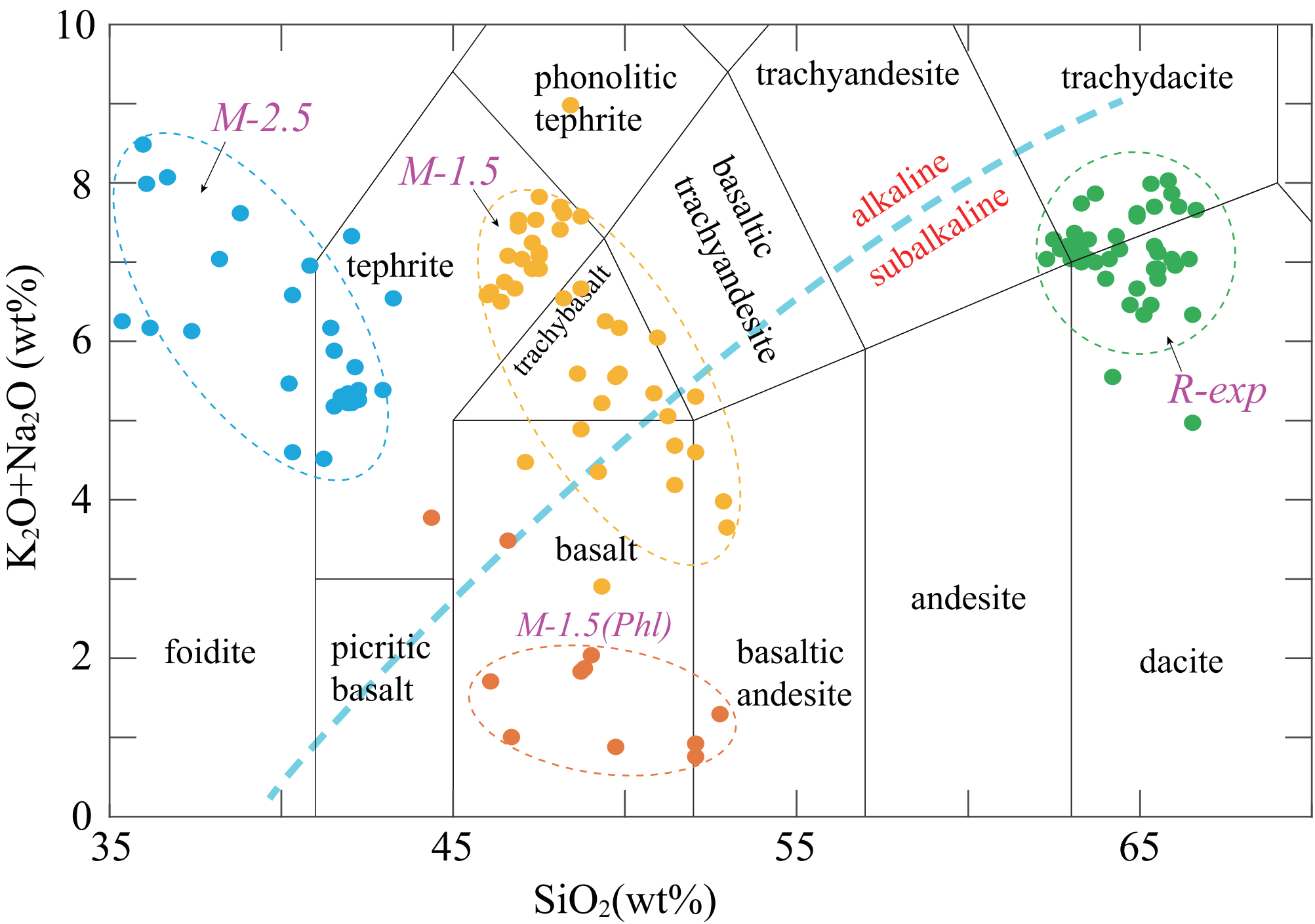
10
8
6
4
2
0
35
45
55
65
K_2O+Na_2O (wt%)
SiO_2(wt%)
M-2.5
M-1.5
M-1.5(Phl)
R-exp
phonolitic tephrite
trachyandesite
trachydacite
basaltic trachyandesite
alkaline
subalkaline
tephrite
trachybasalt
basalt
andesite
foidite
picritic basalt
basaltic andesite
dacite

Figure 4

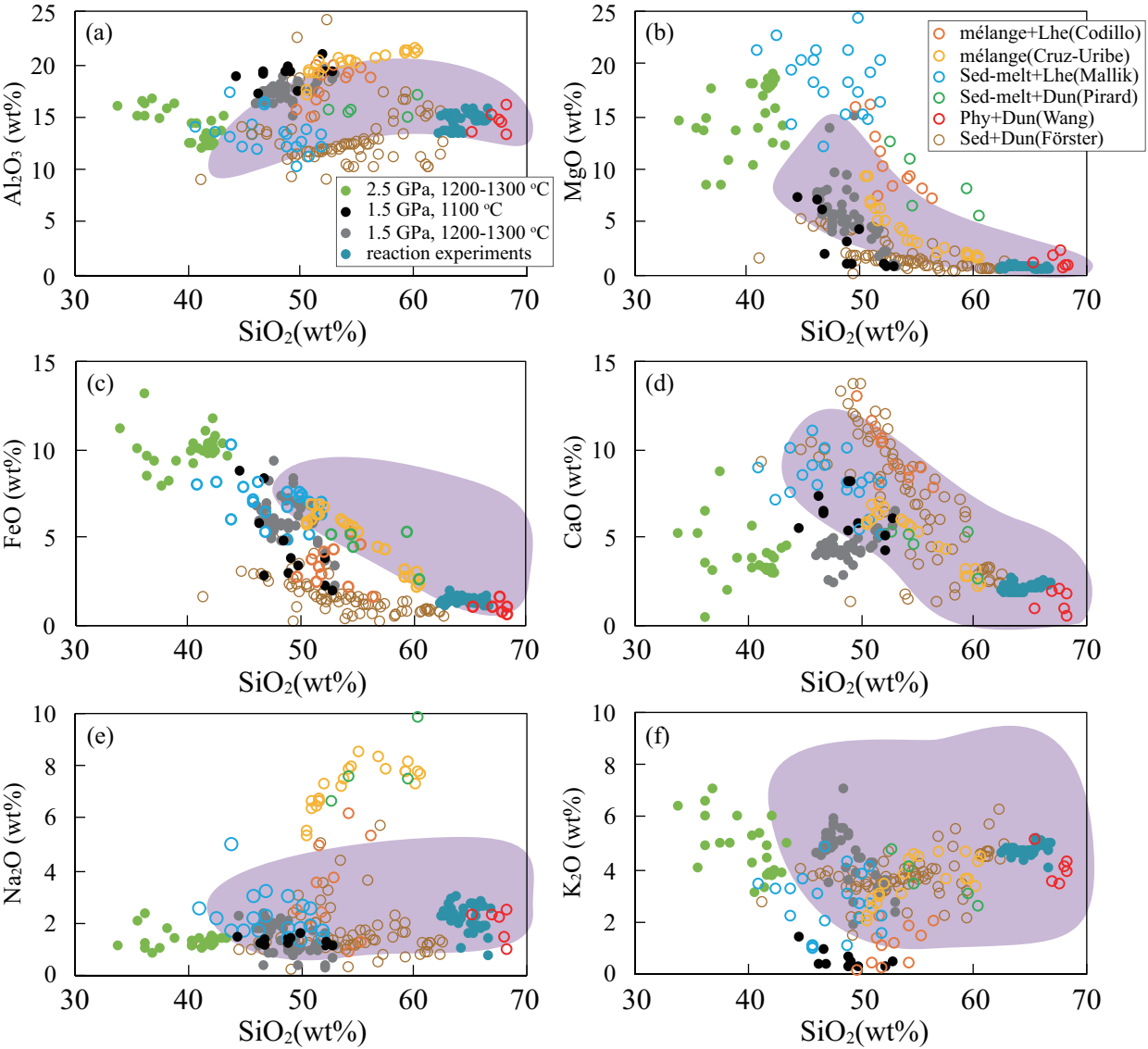
(a)
(b)
(c)
(d)
(e)
(f)
Al2O3 (wt%)
MgO (wt%)
FeO (wt%)
CaO (wt%)
Na2O (wt%)
K2O (wt%)
SiO2(wt%)
2.5 GPa, 1200-1300 °C
1.5 GPa, 1100 °C
1.5 GPa, 1200-1300 °C
reaction experiments
mélange+Lhe(Codillo)
mélange(Cruz-Uribe)
Sed-melt+Lhe(Mallik)
Sed-melt+Dun(Pirard)
Phy+Dun(Wang)
Sed+Dun(Förster)

Figure 5

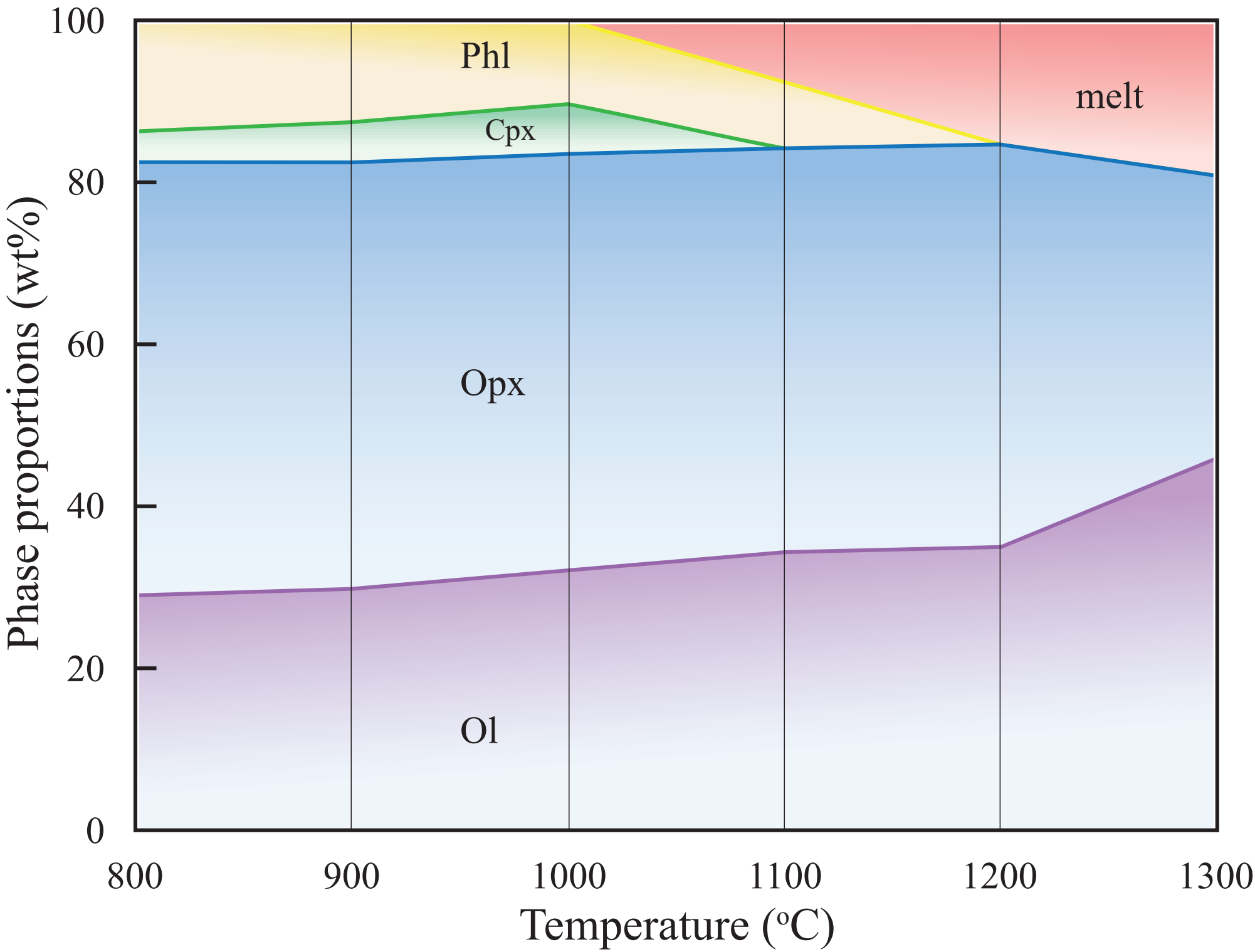
Phl
melt
Cpx
Opx
Ol
100
80
60
40
20
0
800
900
1000
1100
1200
1300
Phase proportions (wt%)
Temperature (°C)

Figure 6

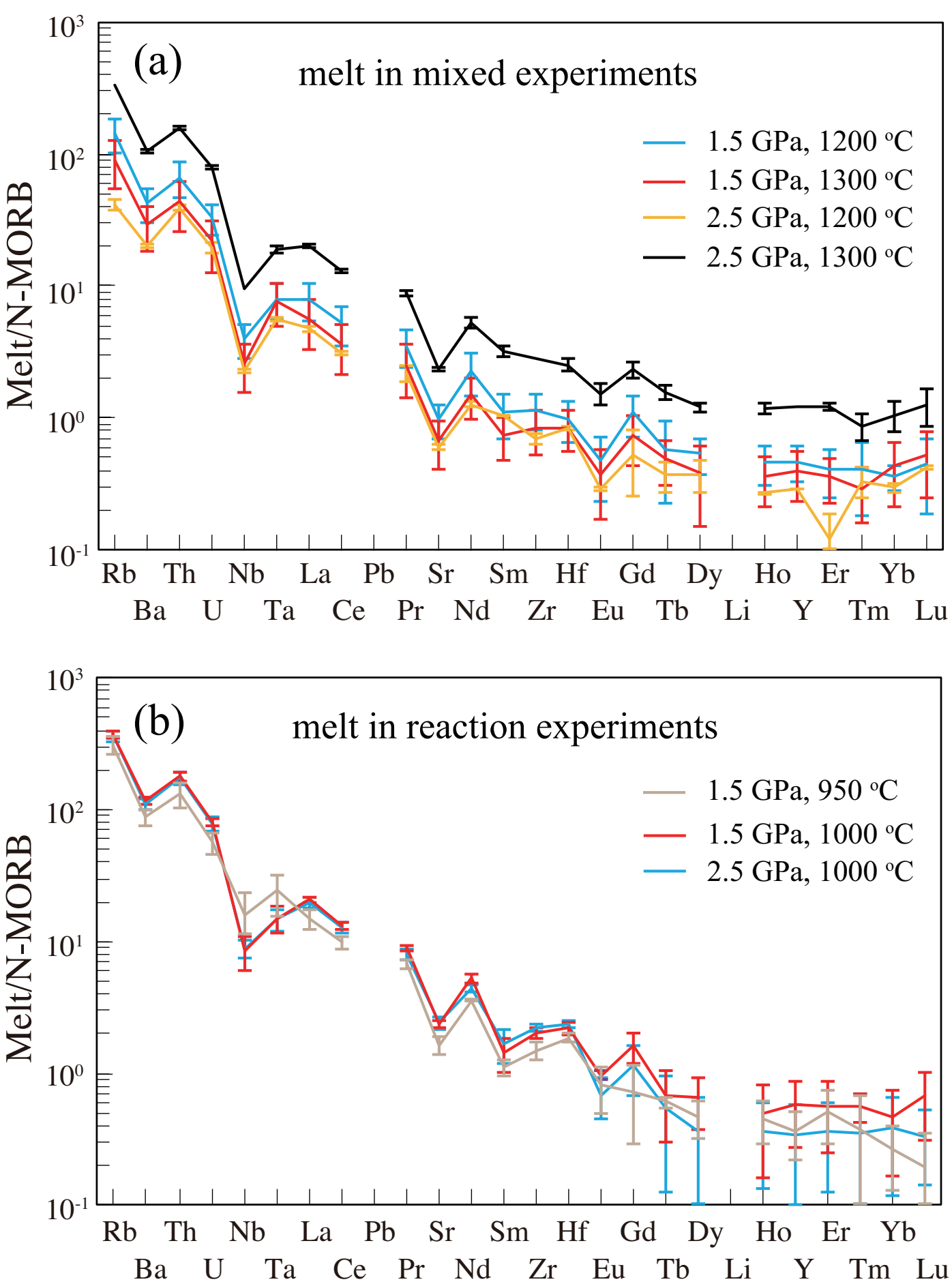
(a)
melt in mixed experiments
1.5 GPa, 1200 °C
1.5 GPa, 1300 °C
2.5 GPa, 1200 °C
2.5 GPa, 1300 °C
Melt/N-MORB
10³
10²
10¹
10⁰
10⁻¹
Rb Th Nb La Pb Sr Sm Hf Gd Dy Ho Er Yb
Ba U Ta Ce Pr Nd Zr Eu Tb Li Y Tm Lu
(b)
melt in reaction experiments
1.5 GPa, 950 °C
1.5 GPa, 1000 °C
2.5 GPa, 1000 °C
Melt/N-MORB
10³
10²
10¹
10⁰
10⁻¹
Rb Th Nb La Pb Sr Sm Hf Gd Dy Ho Er Yb
Ba U Ta Ce Pr Nd Zr Eu Tb Li Y Tm Lu

Figure 7

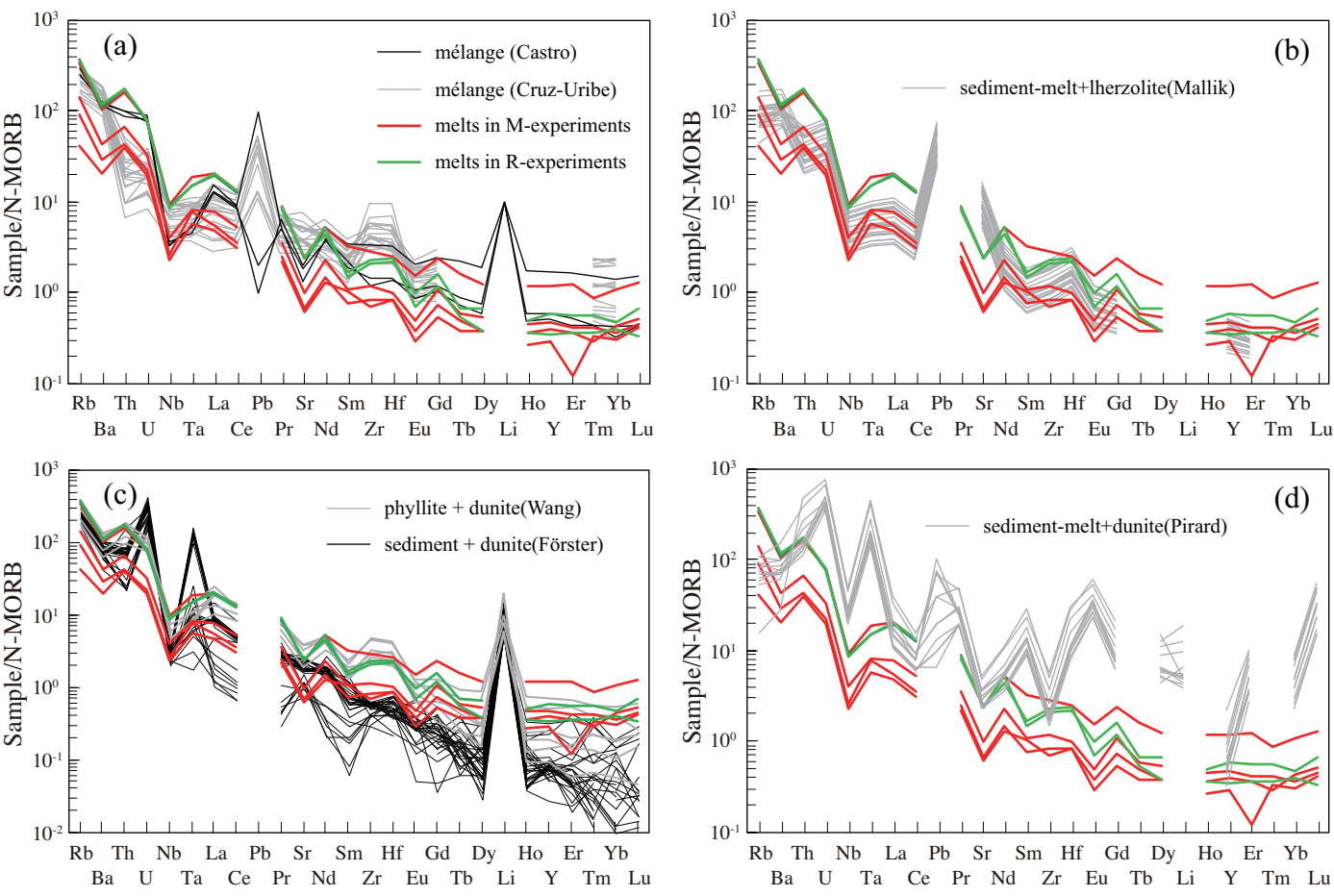
(a)
mélange (Castro)
mélange (Cruz-Uribe)
melts in M-experiments
melts in R-experiments
Sample/N-MORB
(b)
sediment-melt+lherzolite(Mallik)
(c)
phyllite + dunite(Wang)
sediment + dunite(Förster)
(d)
sediment-melt+dunite(Pirard)
Rb Th Nb La Pb Sr Sm Hf Gd Dy Ho Er Yb
Ba U Ta Ce Pr Nd Zr Eu Tb Li Y Tm Lu

Figure 8

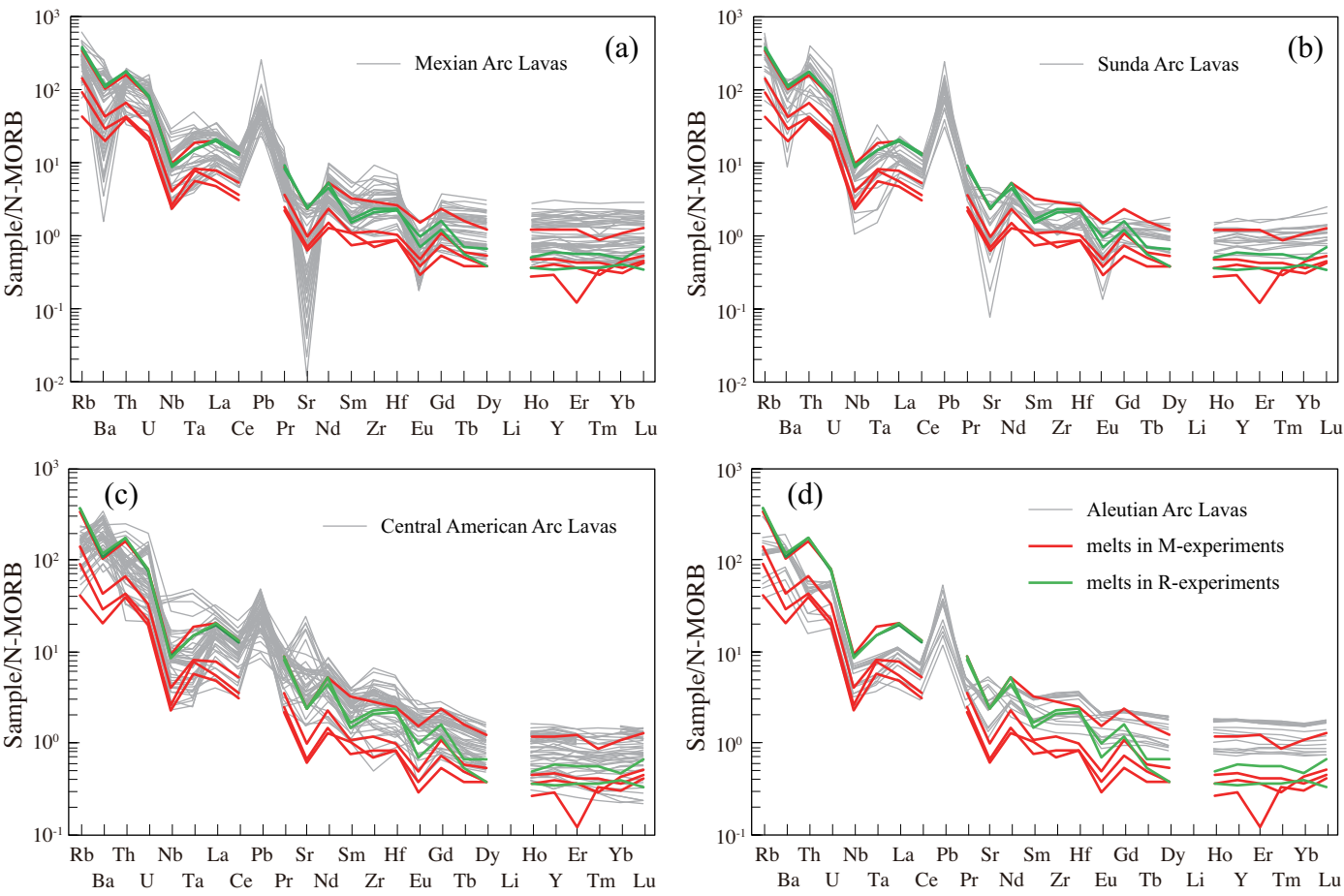
(a)
Mexian Arc Lavas
(b)
Sunda Arc Lavas
(c)
Central American Arc Lavas
(d)
Aleutian Arc Lavas
melts in M-experiments
melts in R-experiments
Sample/N-MORB
Rb Th Nb La Pb Sr Sm Hf Gd Dy Ho Er Yb
Ba U Ta Ce Pr Nd Zr Eu Tb Li Y Tm Lu

Figure 9